Nano Research
2024, 17(5): 3644–3652

ISSN 1998-0124 CN 11-5974/O4
https://doi.org/10.1007/s12274-023-6247-0

Hierarchical Bi/S-modified Cu/brass mesh used as structured highly performance catalyst for CO_2 electroreduction to formate

Tong Dou, Dian Song, Yiping Wang (✉), Xuhui Zhao, Fazhi Zhang, and Xiaodong Lei (✉)

State Key Laboratory of Chemical Resource Engineering, Beijing University of Chemical Technology, Beijing 100029, China

Received: 17 August 2023 / **Revised:** 30 September 2023 / **Accepted:** 6 October 2023

ABSTRACT

Electrocatalytic CO_2 reduction reaction (ECO_2RR) converts CO_2 to high-value chemical products and promotes the carbon cycle. Sulfur (S)-modified copper (Cu) and bismuth (Bi)-based catalysts have been recognized as promising catalysts for ECO_2RR. Both of them are highly active for selective formate generation, however, their poor stability and severe competing hydrogen evolution reaction (HER) remain challenging. Herein, S-doped Cu coated with Bi (Bi/Cu-S) is developed to improve ECO_2RR selectivity to formate. Bi/Cu-S/brass mesh (BM) electrode material for ECO_2RR was prepared by electrodepositing Bi on the surface of Cu-S/BM nanowires obtained from CuS/BM after the electroreduction. The Faradaic efficiency (FE) of the formate reaches the maximum of 94.3% at −0.9 V vs. reversible hydrogen electrode (RHE) with a partial current density as high as $-50.7\ mA\cdot cm^{-2}$ and a yield of $30.7\ mmol\cdot h^{-1}\cdot cm^{-2}$ under 0.5 M $KHCO_3$ electrolyte. Meanwhile, the FE of formate is higher than 90% in the voltage range of −0.8 to −1.0 V vs. RHE. It also shows good stability at −0.9 V vs. RHE with the FE of formate remaining above 93% after a 10 h reaction. Density functional theory (DFT) calculations demonstrate that the Bi/Cu-S structure promotes the adsorption of CO_2 and effectively inhibits HER by enhancing the adsorption of *H to a great extent, improving the selective conversion of CO_2 to formate. This work deepens the understanding of the mechanism of Cu-Bi-based catalysts and S-modified Cu-based catalysts in selective ECO_2RR to formate, and also provides a new strategy for catalyst design.

KEYWORDS

CO_2 electroreduction, Cu-Bi-based catalyst, S-modified Cu catalyst, formate

1 Introduction

Long-term fossil fuel consumption leads to excessive CO_2 emissions, resulting in severe environmental problems around the world. Therefore, achieving carbon emission reduction targets is a considerable challenge for all countries [1–4]. The research on electrocatalytic CO_2 reduction reaction (ECO_2RR) is extensive for its superior transformation ability of CO_2 to value-added products such as CO, HCOOH, CH_4, C_2H_5OH, and C_2H_4 [5–10]. ECO_2RR coupled with renewable electricity is clean, mild and controllable, which is also a promising method to close the carbon loop [11].

Formic acid as a main product of ECO_2RR is a raw material in biopharmaceutical, agricultural, textile, and rubber industries, and is also a high-energy-density molecule applied in formic acid fuel cells [12–14]. Different metal electrocatalysts such as Cd, In, Sn, Hg, and Bi have been widely investigated for ECO_2RR to selectively obtain formate [15–19]. Among them, Bi-based catalysts have received much attention for their low toxicity, low cost, and high H_2 evolution potential for hydrogen evolution reaction (HER) [20]. However, its high overpotential for ECO_2RR to formate and poor electronic conductivity hinder the electrocatalytic performance for selective generation of formate [21]. In addition, Bi metal is fragile, so coating Bi on other metal substrates is beneficial to enhance the stability of the catalyst [21]. Meanwhile, the introduction of a second metal modulates the electronic structure of the catalyst thus enhancing the activity, selectivity, and stability for ECO_2RR. Thus, Cu as a catalyst for ECO_2RR exhibiting tunable selectivity and high electronic conductivity is introduced into Bi to form bimetallic Bi-Cu materials, which show good activity for ECO_2RR to formate. It has been reported that incorporating Cu into Bi nanocrystals modulates the local electronic environment of Bi atoms, changing the formation path of HCOOH from *COOH to *OCHO intermediate, and suppressing the formation of by-products CO and H_2. It has exhibited the highest Faradaic efficiency (FE) for formate of 90.9% at −1.2 V vs. reversible hydrogen electrode (RHE) [22]. Electron-rich Bi nanosheet obtained by growing Bi on Cu nanodendrite has been used in ECO_2RR. The electron-rich Bi facilitates the formation of $CO_2\cdot^-$ and enhances the adsorption of *OCHO intermediate, thus obtaining better selectivity of formate. It has been revealed that the highest FE for formate of 92.5% at −1.0 V vs. RHE is achieved [19].

Furthermore, S-modified Cu catalysts have inherent activity for ECO_2RR to selectively generate formate. S-doped Cu catalyst has been reported to show FE for formate of 75% at −0.9 V vs. RHE [23]. The experiment confirms that doping S inhibits the formation of *CO intermediate and changes the adsorption strength of intermediate HCOO*, which promotes the formation of formate and inhibits the formation of *COOH and *CO, thus improving the formate selectivity. Based on our previous study on CuS nanosheets/brass mesh (BM) catalyst applied in ECO_2RR, CuS/BM is reduced during the electroreduction process, and is

---

Address correspondence to Xiaodong Lei, leixd@mail.buct.edu.cn; Yiping Wang, wangyiping@buct.edu.cn

transformed to S-doped Cu nanowires/BM where S is beneath the surface Cu^0 layer during the initial reaction process [24]. Compared with Cu, the presence of S lowers the adsorption strength of *OCHO and *COOH, promoting the formation of formate. CuS/BM shows an FE of 70% for formate at –0.7 V vs. RHE. However, the reduction of CuS during ECO_2RR results in a low total FE of less than 100%, and the oxidation of surface Cu decreases its reusability. Therefore, it is important for S-modified Cu-based catalysts to improve product selectivity while maintaining catalyst stability in ECO_2RR.

Considering the synergistic effect of bimetallic Bi-Cu and the effect of S for improving the activity for ECO_2RR, we electrodeposited Bi on the surface of Cu-S/BM nanowires prepared by electroreduction of CuS/BM to form Bi/Cu-S/BM electrode materials for ECO_2RR, in order to obtain high formate selectivity with good stability. The presence of Cu-S improves the electron transmission rate of the catalyst, meanwhile, the Bi-coated Cu-S structure protects the stable presence of S and prevents the air oxidation of Cu. The unique structure also improves selective formate production through electronic structure regulation. The adsorption strength of reaction intermediates for HCOOH, CO, and H_2 products and the Gibbs free energy of HCOOH, CO, and H_2 generation on the surfaces of Bi/Cu-S, Bi/Cu, and Bi atomic models were analyzed by density functional theory (DFT) calculations.

2 Experimental

2.1 Chemicals and materials

$KHCO_3$ (Aladdin Ltd.), $Na_2S{\cdot}9H_2O$ (Macklin), S powder (Alfa Aesar), NaOH (Macklin), hydrochloric acid (Beijing Chemical Works), C_2H_5OH (Beijing Chemical Works), $Bi(NO_3)_3{\cdot}5H_2O$ (Aladdin Ltd.), and $Na_3C_6H_5O_7{\cdot}2H_2O$ (Beijing Chemical Works) are all analytical reagents. Brass mesh (200 mesh) was provided by Daoguan Rubber & Plastic Hardware, Inc. Shanghai.

2.2 Synthesis of Bi/Cu-S/BM and Bi/BM

CuS/BM nanosheet arrays were prepared by the chemical bath deposition method. $Na_2S{\cdot}9H_2O$ (0.10 $mol{\cdot}L^{-1}$), S (0.10 $mol{\cdot}L^{-1}$), and NaOH (0.10 $mol{\cdot}L^{-1}$) were dissolved in deionized water with continuous aeration of N_2 and stirring to form polysulfide solution. The BM (3 cm × 4 cm, 200 mesh) was cleaned by ultrasonic treatment in dilute hydrochloric acid, deionized water, and anhydrous ethanol, respectively. It was placed in polysulfide solution (50 mL) in a thermostat water bath kept at 30 °C for 24 h. Then, it was washed with deionized water and dried.

To obtain Cu-S/BM and Bi/Cu-S/BM, a cathodic transformation was carried out by a chronopotentiometry method with a three-electrode system using an electrochemical workstation (CHI660E, CH Instruments Inc., Shanghai). Cu-S/BM was prepared by the electroreduction of CuS/BM. The prepared CuS/BM (2 cm × 3 cm), graphite rod and Ag/AgCl electrode (3 $mol{\cdot}L^{-1}$ KCl) worked as working, counter, and reference electrodes, respectively. $Na_3C_6H_5O_7{\cdot}2H_2O$ (0.10 $mol{\cdot}L^{-1}$) was dissolved in 50 mL of hydrochloric acid solution (1.20 $mol{\cdot}L^{-1}$) as the electrolyte. After the cathodic transformation at a constant current of –15 mA for 6 min, the Cu-S/BM electrode was obtained. It was washed with deionized water and stored in deionized water to prevent surface oxidation. Then, $Bi(NO_3)_3{\cdot}5H_2O$ (0.05 $mol{\cdot}L^{-1}$) was dissolved in the above-mentioned hydrochloric acid solution as the electrolyte. Cu-S/BM (2 cm × 3 cm), graphite rod, and Ag/AgCl electrode (3 $mol{\cdot}L^{-1}$ KCl) worked as working, counter, and reference electrodes, respectively. After the cathodic transformation at a constant current of –15 mA for 6 min, Bi was electrodeposited on the surface of Cu-S/BM, and the electrode was labelled as Bi/Cu-S/BM.

For comparison, Bi/BM was prepared by direct electrodeposition of Bi on a BM (2 cm × 3 cm). $Na_3C_6H_5O_7{\cdot}2H_2O$ (1.20 $mol{\cdot}L^{-1}$) and $Bi(NO_3)_3{\cdot}5H_2O$ (0.05 $mol{\cdot}L^{-1}$) were dissolved in the hydrochloric acid solution (1.20 $mol{\cdot}L^{-1}$) as the electrolyte. BM (2 cm × 3 cm), graphite rod, and Ag/AgCl electrode (3 $mol{\cdot}L^{-1}$ KCl) worked as working, counter, and reference electrodes, respectively. After the cathodic transformation at a constant current of –15 mA for 6 min, Bi/BM was obtained.

2.3 Characterization

X-ray diffraction (XRD) was characterized by Bruker D8A25 (Cu target, ceramic X-ray tube, 2.2 kW) with a scanning speed of $10°{\cdot}min^{-1}$. Raman spectrometer LabRAM Aramis with a He-Ne laser wavelength of 532 nm was used. X-ray photoelectron spectroscopy (XPS) measurements were performed on an axis supra X-ray photoelectron spectrometer (Al *Kα* radiation, 2×10^{-9} Pa). The morphology of the sample was observed by scanning electron microscopy (SEM, Zeiss SUPRA 55) equipped with an INCA Energy 350 ADD energy dispersive spectrometer (EDS). High-resolution transmission electron microscopy (HRTEM, JEM-2010) at a voltage of 200 kV was used to determine the crystal structure. An inductively coupled plasma optical emission spectrometer (ICP-OES, ICP-6300, Thermo Fisher Scientific, USA) was used to measure the element contents of the samples.

2.4 Electrochemical reduction of CO_2 and product analyses

The electrochemical properties were tested by an electrochemical workstation (CHI 660E). A gas-tight H-type electrolytic cell and the three-electrode system were used. 30 mL electrolyte (0.5 $mol{\cdot}L^{-1}$ $KHCO_3$) was poured into cathodic and anodic compartments, respectively, which were separated by a cation exchange membrane (Nafion 115, DuPont). Bi/Cu-S/BM or Bi/BM (1 cm × 1 cm), Ag/AgCl electrode (in 3 $mol{\cdot}L^{-1}$ KCl solution), and graphite rod were used as working, reference and counter electrodes, respectively. All potentials mentioned were relative to the RHE, which is converted to the potential relative to the Ag/AgCl electrode by Eq. (1) as follows

$$E(\text{V vs. RHE}) = E(\text{V vs. Ag/AgCl}) + 0.21\ \text{V} + 0.0592 \times \text{pH} \quad (1)$$

All potentials are not *IR*-corrected. Linear sweep voltammetry (LSV) was carried out at a scan rate of 5 $mV{\cdot}s^{-1}$. Ar (99.999%) or CO_2 gas (99.999%) was continuously flowed through in the electrolyte at a flow rate of 20 $mL{\cdot}min^{-1}$. The pH values of Ar-saturated and CO_2-saturated electrolytes were 8.3 and 7.2, respectively. The electrochemical double-layer capacitance (C_{dl}) was obtained by CV curves at non-Faradic region. Electrochemical impedance spectra (EIS) were recorded over a frequency of 0.01 Hz to 10 kHz. The gas products were analyzed online every 30 min by gas chromatography (Agilent 8890) equipped with HP-PLOT Al_2O_3 S, 5A molecular sieve, and HayesepQ columns. The liquid products were analyzed after chronoamperometry of 90 min by high-performance liquid chromatography (Agilent 1260) equipped with an Agilent Hi-Plex H column and ultraviolet spectrophotometric detector. The eluent was the H_2SO_4 solution (5 $mmol{\cdot}L^{-1}$) with the flow rate of 0.6 $mL{\cdot}min^{-1}$ and the temperature of 65 °C.

The FE was calculated by Eq. (2), where n is the mole number of the product; z is the electron transfer number of one molecule product; F is the Faraday constant, and Q is the total charge

$$\mathrm{FE}\ (\%) = znF/Q \tag{2}$$

2.5 Computational details

All DFT calculations were performed by Generalized gradient approximation (GGA) with a Perdew–Burke–Ernzerhof (PBE) using the Cambridge Sequential Total Energy Package (CASTEP) of Materials Studio. The detailed computational information is displayed in Text S1 in the Electronic Supplementary Material (ESM).

3 Results and discussion

3.1 Synthesis and structure of the catalysts

As shown in Fig. 1(a), Bi/Cu-S/BM is synthesized by the electrodeposition of Bi on the surface of Cu-S/BM, which is electrochemically reduced from CuS/BM. Raman peaks of CuS/BM in Fig. 1(b) at about 126.9, 264.5, and 474.3 cm^{-1} match closely with the reported Raman spectrum of CuS crystal at 137.3, 261.9, and 471.0 cm^{-1}, respectively [25]. Among these peaks, the peak at 474.3 cm^{-1} is assigned to the symmetric stretching vibration of the S–S bond, according to the S_2 groups of crystal structure of CuS [26, 27]. The vibration at 126.9 and 264.5 cm^{-1} is attributed to the weak Cu–S stretching bonds [28]. For Cu-S/BM, the disappearance of the CuS signals in its Raman spectrum indicates that the surface of CuS is electrochemical reduced to Cu. The XRD spectra of CuS/BM and Cu-S/BM in Fig. 1(c) show that the diffraction peaks at 42.3°, 49.2° and 72.4° correspond to the standard diffraction peaks of $Cu_{0.64}Zn_{0.36}$ (PDF#06-0464) for the brass. The peaks at 29.3°, 32.9°, 47.9°, and 52.7° in CuS/BM are ascribed to CuS (PDF#06-0464), and these peaks disappear in the XRD spectrum of Cu-S/BM, indicating that CuS is electrochemical reduced, which is consistent with the Raman result. The loading amount of CuS of CuS/BM is ~ 0.54 mg·cm^{-2}, which is calculated by the mass difference value before and after the synthesis of CuS/BM. The diffraction peaks of Bi/Cu-S/BM and Bi/BM at 27.2°, 38.0°, 39.6°, 48.7°, and 56.0° match well with the (012), (104), (110), (202), and (024) planes of Bi (PDF#44-1246) respectively, where the diffraction peak at 56.0° is shifted compared to the standard peak of (024) plane at 55.6° due to the interaction between Bi and Cu. The Raman and XRD results indicate the successful synthesis of Bi/Cu-S/BM. In addition, the loading of Bi (~ 3.81 mg·cm^{-2}) and S (~ 0.04 mg·cm^{-2}) in Bi/Cu-S/BM were further confirmed by ICP-OES.

The morphologies of CuS/BM, Cu-S/BM, and Bi/Cu-S/BM are shown in SEM images. As displayed in Figs. 2(a)–2(i), CuS/BM nanosheets with the diameter of ~ 1 μm are transformed into nanowires when it is reduced to Cu-S/BM. For Bi/Cu-S/BM, Bi particles are uniformly electrodeposited onto the surface of Cu-S/BM.

The surface structures of Cu-S/BM and Bi/Cu-S/BM were further analyzed by HRTEM. As shown in Fig. 3(a), most of the Cu-S/BM surface is Cu(111) plane with the lattice spacing of 0.20 nm, leaving a small area of CuS(102) plane with the lattice spacing of 0.30 nm, and the lattice spacing of 0.25 nm is ascribed to $Cu_2O(111)$ [29–31]. Although the samples were kept in an N_2 atmosphere before the characterization of HRTEM, the Cu-S/BM sample is inevitably exposed to air before the characterization leading to the oxidation of Cu. The elemental distribution of Cu-S/BM is shown in Fig. 3(b), indicating that Cu and a small amount of S are uniformly distributed in the sample, and the EDS results indicate that S content is 5.2% (Table S1 and Fig. S1 in the ESM). As shown in Fig. 3(c), the HRTEM image of Bi/Cu-S/BM shows that the surface is Bi(012) plane with a lattice spacing of 0.33 nm [32]. The elemental mappings in Fig. 3(d) and Fig. S2 in the ESM indicate that Bi, Cu, and a small amount of S elements are uniformly distributed in the sample, and the EDS results show that S content is 4.3% (Table S2 and Fig. S3 in the ESM). The HRTEM characterization further confirms that Bi/Cu-S/BM is successfully synthesized.

XPS analysis was carried out to further investigate the surface atomic composition and valence state of CuS/BM, Cu-S/BM, and Bi/Cu-S/BM. As shown in Fig. 4(a), Cu 2p XPS of CuS/BM is deconvoluted into the couple peaks. Peaks at 932.3 and 952.1 eV ascribe to $2p_{3/2}$ and $2p_{1/2}$ orbital peaks of Cu^+ or Cu^0, the peaks at 934.2 and 954.2 eV ascribe to Cu^{2+}, and peaks at 942.9 and 962.8 eV ascribe to the satellite peaks of Cu^{2+} [21, 24]. Meanwhile, Fig. 4(b) shows the S 2p XPS of CuS/BM. Peaks at 161.6 and 162.8 eV are attributed to the $2p_{3/2}$ and $2p_{1/2}$ of S^{2-} corresponding to the Cu–S bond. Peaks at 163.4 and 164.6 eV are attributed to $2p_{3/2}$ and $2p_{1/2}$ orbital peaks of the S_2 unit in CuS [8]. The Cu 2p, S

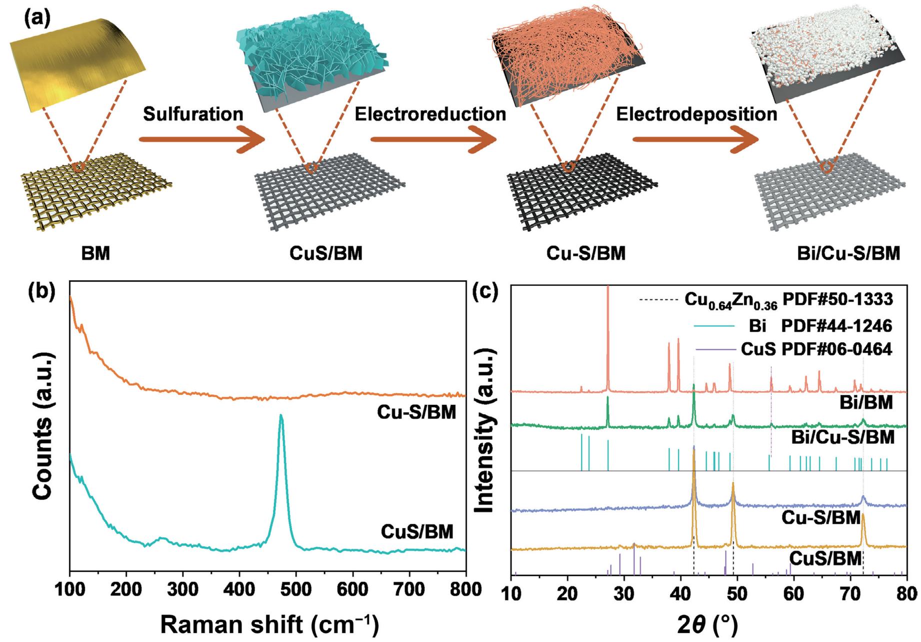

Figure 1 (a) Schematic illustration for the fabrication of Bi/Cu-S/BM. (b) Raman spectra of CuS/BM and Cu-S/BM. (c) XRD patterns of CuS/BM, Cu-S/BM, Bi/Cu-S/BM, and Bi/BM.

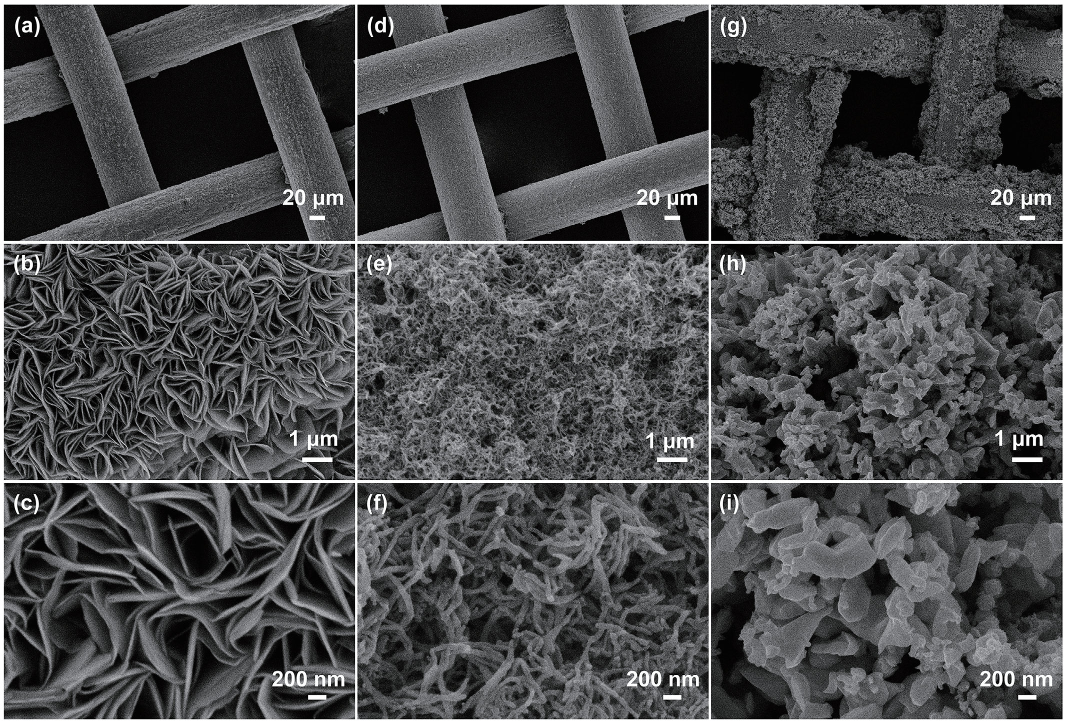

Figure 2 SEM images of ((a)–(c)) CuS/BM, ((d)–(f)) Cu-S/BM, and ((g)–(i)) Bi/Cu-S/BM.

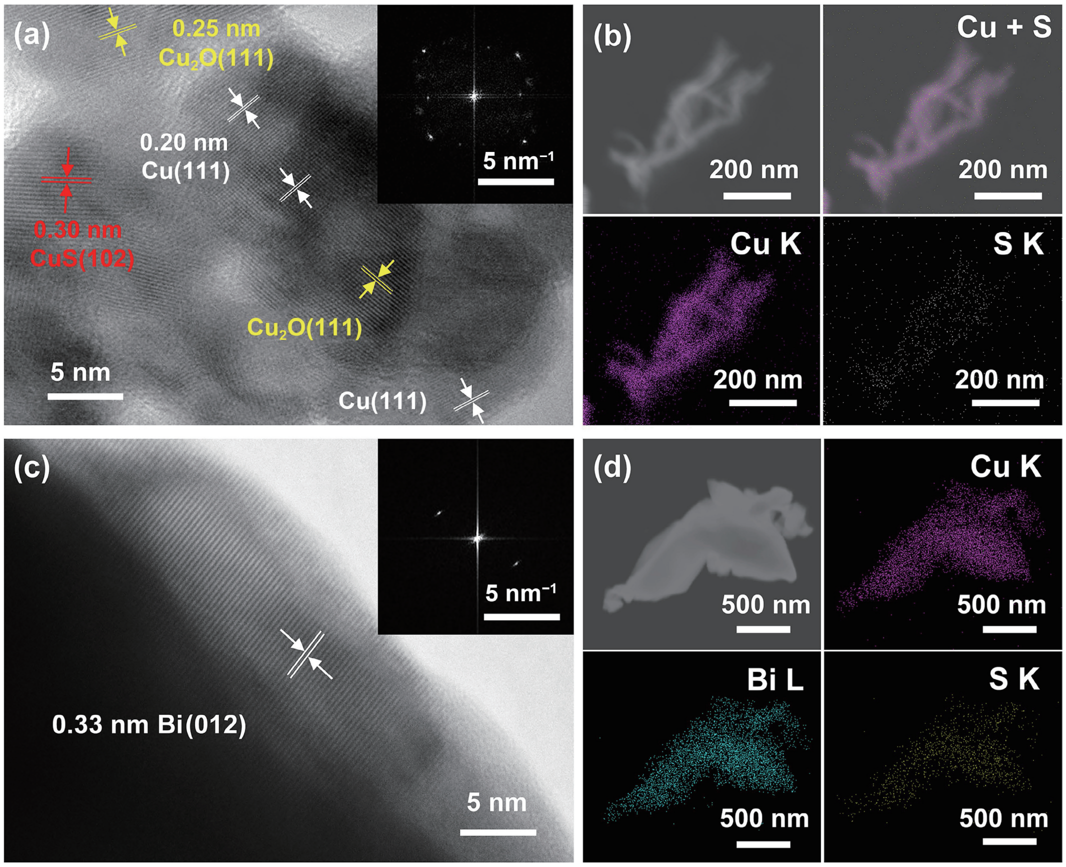

Figure 3 HRTEM images and elemental mappings of ((a) and (b)) Cu-S/BM and ((c) and (d)) Bi/Cu-S/BM, respectively.

2p, and Bi 4f spectra of Cu-S/BM and Bi/Cu-S/BM are shown in Figs. 4(c) and 4(d), respectively. The Cu 2p and S 2p spectra of Cu-S/BM indicate that Cu exists mainly as Cu^0. Peaks at 931.9 and 951.7 eV correspond to $2p_{3/2}$ and $2p_{1/2}$ of Cu^0, demonstrating the surface CuS/BM is reduced to Cu^0 [8, 24]. For Bi/Cu-S/BM, after the electrodeposition of Bi on Cu-S/BM, a positive shift of Cu 2p is observed for Cu^0, indicating that Cu transfers electrons to Bi. Cu LMM Auger electron spectroscopy in Fig. S4 in the ESM further clarifies the state of Cu element of CuS/BM, Cu-S/BM, and Bi/Cu-S/BM. The peaks at 568.0, 569.1, and 569.9 eV are attributed to Cu^0, Cu^{2+}, and Cu^{1+}, respectively [33]. The results demonstrate the production of positively charged metallic $Cu^{\delta+}$ species ($0 < \delta < 1$) due to the lower electron concentration of Cu atoms on the Bi/Cu-S/BM surface compared to Cu-S/BM, which are consistent with the results of Cu 2p analysis [34, 35]. Bi 4f spectrum shows that peaks at 159.0 and 162.4 eV are ascribed to Bi $4f_{7/2}$ and $4f_{5/2}$ of Bi^{3+}

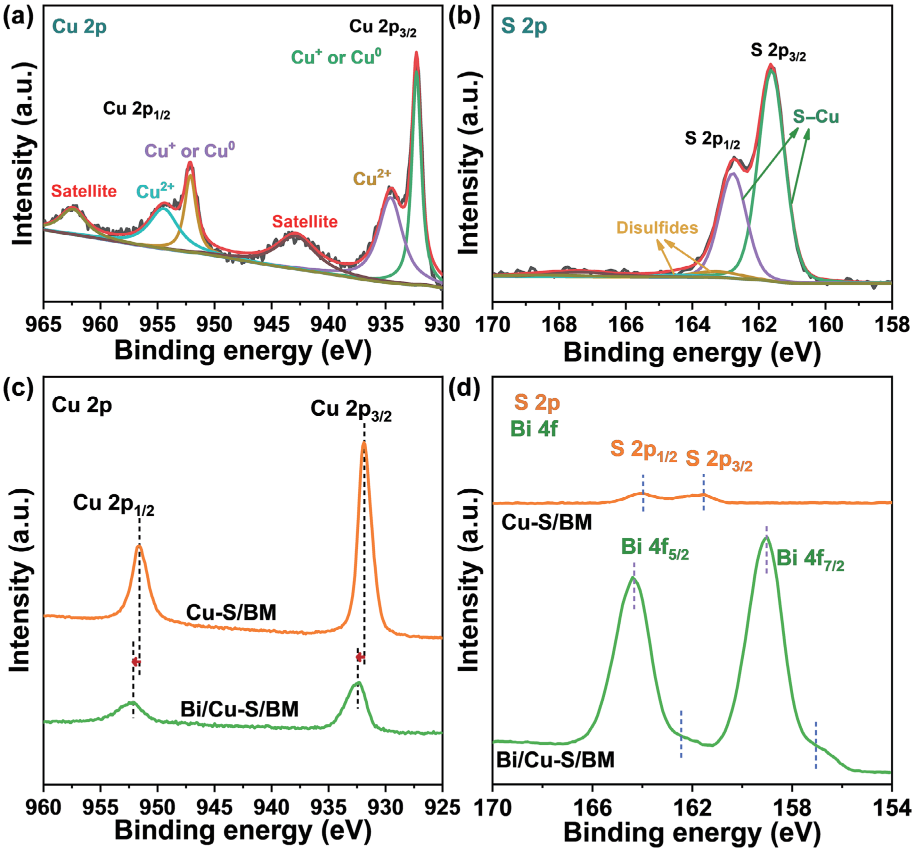

Figure 4 XPS analyses of ((a) and (b)) CuS/BM and ((c) and (d)) Cu-S/BM and Bi/Cu-S/BM.

for Bi_2O_3, which is due to the oxidation of Bi in the air, and peaks at 157.1 and 162.4 eV correspond to Bi^0 [36]. XPS results indicate that Bi is successfully deposited on Cu-S/BM and interacts with Cu obtaining more electrons.

3.2 The performance of ECO_2RR

Figure 5(a) shows the LSV curves of Bi/Cu-S/BM and Bi/BM in Ar and CO_2 saturated 0.5 M $KHCO_3$ electrolyte, respectively. The results indicate that Bi/Cu-S/BM has a lower onset potential than Bi/BM in CO_2-saturated electrolytes and the total current density is higher than that of Bi/BM over the potential range of −0.4 to −1.2 V. Meanwhile, the LSV curves of Bi/Cu-S/BM and Bi/BM almost overlapped in the Ar-saturated electrolyte, indicating that Bi/Cu-S/BM has the superior activity of ECO_2RR than that of Bi/BM. The chronoamperometry *i*–*t* curves of Bi/Cu-S/BM in Fig. 5(b) show that the current density becomes the higher with the potential increasing. Meanwhile, it decreases with the time increasing at −1.2 V, because the large current density causes the catalyst structure to be destroyed and the catalyst is partially dropped. When the potential is lower than 1.2 V, the current density remains stable. As shown in Fig. 5(c), the products of ECO_2RR using Bi/Cu-S/BM as the electrocatalyst are $HCOO^-$, CO, and H_2. The FEs of the main product $HCOO^-$ are higher than 90% over −0.8 to −1.0 V, reaching the maximum of 94.3% at −0.9 V. Meanwhile, the partial current density of $HCOO^-$ is $-50.7\ mA\cdot cm^{-2}$ and the yield of $HCOO^-$ is $30.7\ mmol\cdot h^{-1}\cdot cm^{-2}$ at −0.9 V. The FEs of CO are all lower than 1.5% at different potentials, which can be negligible. Figure 5(d) displays that the yield of formate reaches the maximum of $63.9\ mmol\cdot h^{-1}\cdot cm^{-2}$ at −1.1 V. Figure 5(e) shows the stability test of Bi/Cu-S/BM at −0.9 V for 10 h, indicating that the current density remains stable at about $-53.4\ mA\cdot cm^{-2}$, and the FE of $HCOO^-$ also remains stable above 93% after 10 h.

The performance of ECO_2RR for Bi/Cu-S/BM in this work is compared with the performance of Bi-based and S-modified Cu-based catalysts reported in previous literature [8, 19, 22–24, 37–50]. As shown in Table S3 in the ESM, Bi/Cu-S/BM achieves the $FE_{formate}$ higher than 90% at a relatively low potential of −0.8 V, which is better than all Cu-S-based catalysts. At −0.9 V, it achieves the $FE_{formate}$ higher than 94%, a large local current density of $-50.7\ mA\cdot cm^{-2}$ and a high yield of $30{,}741.3\ \mu mol\cdot h^{-1}\cdot cm^{-2}$, which is better than the performance of most Bi-based catalysts.

To analyze the effect of Cu-S of Bi/Cu-S/BM on the performance, Bi/BM was used as a comparison sample to analyze its products, and the results are shown in Fig. S5 in the ESM. The chronoamperometry *i*–*t* curves in Fig. S5(a) in the ESM show that the current densities of Bi/BM decrease rapidly with increasing reaction time at −1.1 and −1.2 V, indicating that Bi/BM is unstable at high current densities. At the same current density of $-120\ mA\cdot cm^{-2}$, the current density of Bi/Cu-S/BM changes less in the same reaction time, indicating that Bi/BM is more easily destroyed than Bi/Cu-S/BM. As shown in Fig. S5(b) in the ESM, the products of ECO_2RR using Bi/BM as the electrocatalyst are $HCOO^-$, CO, and H_2. The FEs of the main product $HCOO^-$ are higher than 85% at −0.9 to −1.1 V, reaching the maximum of 89.5% at −0.9 V. The partial current density of $HCOO^-$ is $-40.1\ mA\cdot cm^{-2}$ and the yield of $HCOO^-$ is $21.8\ mmol\cdot h^{-1}\cdot cm^{-2}$. The FEs of the CO are lower than 1.4%, which can be negligible compared with $HCOO^-$. Figure S5(c) in the ESM displays that the yield of formate reaches the maximum of $52.9\ mmol\cdot h^{-1}\cdot cm^{-2}$ at −1.2 V. In summary, compared with Bi/BM, Bi/Cu-S/BM exhibits the higher formate selectivity and yield at lower potentials, while generating less H_2 as a by-product.

In addition, the electrochemical active surface area (ECSA) was estimated by measuring the C_{dl}. As shown in Figs. S6(a)–S6(c) in the ESM, Bi/Cu-S/BM has larger C_{dl} ($3.09\ mF\cdot cm^{-1}$) than that of Bi/BM ($2.20\ mF\cdot cm^{-1}$), indicating that Bi/Cu-S/BM has the more active sites for ECO_2RR. In addition, as shown in Fig. S6(d) in the ESM, the EIS results indicate that Bi/Cu-S/BM has the smaller

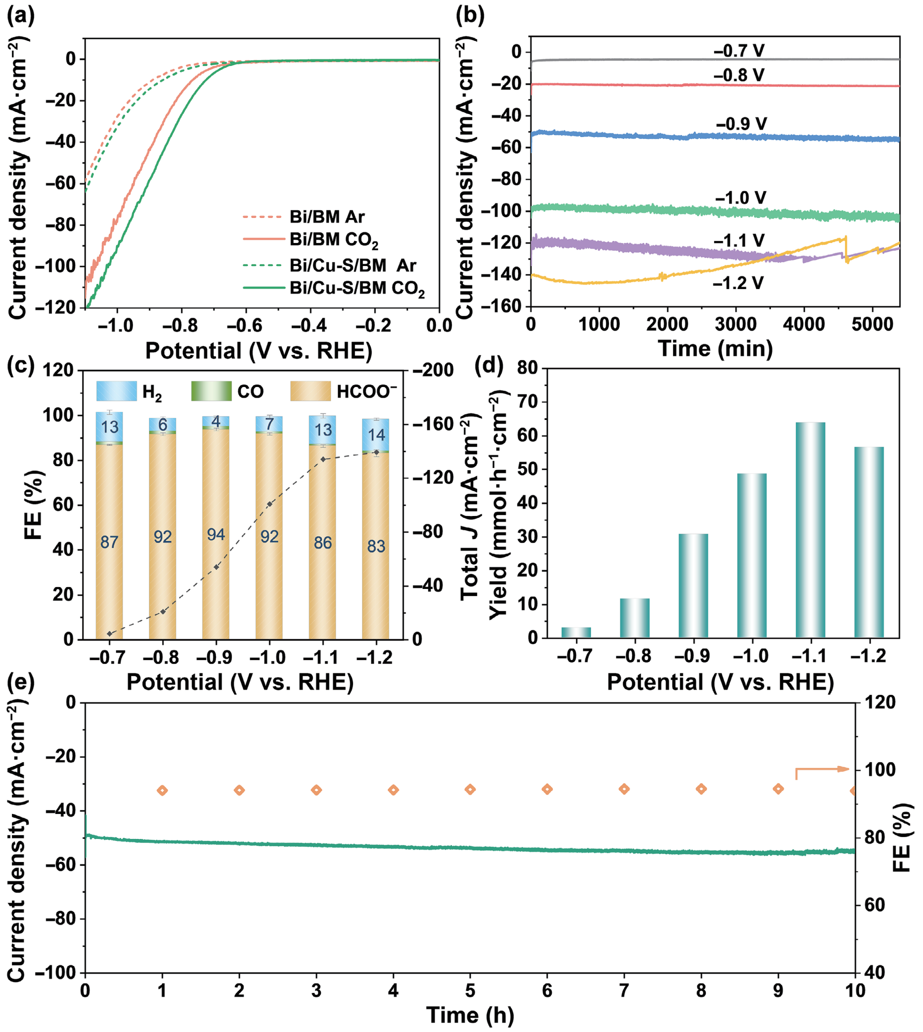

Figure 5 (a) LSV curves of Bi/BM and Bi/Cu-S/BM. (b) Chronoamperometric *i*–*t* data of Bi/Cu-S/BM at potentials over the range of −0.7 to −1.2 V. (c) FEs and (d) yields of formate for Bi/Cu-S/BM at different applied potentials. (e) Stability test of Bi/Cu-S/BM at −0.9 V.

interfacial charge transfer resistance (R_{ct} = 2.18 Ω·cm^2) compared with Bi/BM (R_{ct} = 2.55 Ω·cm^2), demonstrating the faster interfacial charge transfer. The fitting equivalent circuit diagram and the fitting parameters are shown in Fig. S6(d) and Table S4 in the ESM, respectively.

3.3 Mechanism for the formation of HCOO$^-$

To further investigate the mechanism of selective HCOO$^-$ generation of ECO$_2$RR using Bi/Cu-S/BM as the electrocatalyst, the reaction pathways were investigated by DFT calculation. Atomic models of Bi(012)/Cu(111)-S, Bi(012)/Cu(111), and Bi(012) were constructed based on the structural design of Bi/Cu-S/BM and its structural characterization, and their top and side views are shown in Figs. 6(a)–6(c). Figures 6(d)–6(f) show the Gibbs free energy diagrams for the generation of CO and HCOOH from CO$_2$ on the surfaces of Bi(012)/Cu(111)-S, Bi(012)/Cu(111), and Bi(012), respectively. All of Bi(012)/Cu(111)-S, Bi(012)/Cu(111), and Bi(012) favour the conversion of CO$_2$ to HCOOH rather than CO. The Δ*G* required for adsorption and activation of CO$_2$ on the Bi(012)/Cu(111)-S and Bi(012)/Cu(111) surfaces are both 0.29 eV, which is lower than the energy barrier for the Bi(012) surface (Δ*G* = 0.31 eV). The formation of *CO from *COOH on the Bi(012)/Cu(111)-S surface requires Δ*G* of 4.13 eV, which is 2.88 eV higher than that of Bi(012)/Cu(111) (Δ*G* = 1.25 eV). Therefore, the presence of S inhibits the formation of *CO from *COOH. Figure 6(g) displays the comparison of the adsorption energies (Δ*E*) for CO$_2$, intermediates *COOH, *OCHO, *CO, and *H on the surfaces of Bi(012)/Cu(111)-S, Bi(012)/Cu(111), and Bi(012). The results show that the adsorption of CO$_2$ and all intermediates are enhanced on the Bi(012)/Cu(111) and Bi(012)/Cu(111)-S surfaces compared with Bi(012), and the enhanced adsorption of *COOH facilitates their further reaction to generate *CO, which explains that the FEs of CO using Bi/Cu-S/BM electrode (< 1.5%) in the experimental result are slightly higher than that of Bi/BM (< 1.4%). Among them, the enhanced adsorption of *H is much higher than that of the other intermediates, and *H is most strongly adsorbed on the Bi(012)/Cu(111)-S surface, which is the reason for the suppressed HER using Bi/Cu-S/BM compared with Bi/BM in ECO$_2$RR. Figure 6(h) shows the Gibbs free energy of H$_2$ formation on the surfaces of three models, indicating that the formation of H$_2$ from *H is more difficult on the Bi(012)/Cu(111)-S surface, which requires Δ*G* of 2.24 eV, higher than that of Bi(012)/Cu(111) (Δ*G* = 1.85 eV) and Bi(012) (Δ*G* = 0.4 eV), which is responsible for the inhibition of HER. Thus, Bi/Cu-S/BM enhances selective formate generation by promoting the adsorption of CO$_2$ and suppressing HER.

In addition, the structural stability of Bi/Cu-S/BM after the chronoamperometry test for 10 h at −0.9 V was characterized by XRD and SEM. As shown in Fig. S7(a) in the ESM, the XRD spectra show that the structure of Bi/Cu-S/BM after the reaction is the same as that before the reaction, without significant changes. Figures S7(b)–S7(d) show the SEM images after the reaction. The morphology remains uniform particles, similar to the morphology before the reaction, and the EDS results show that the S content is

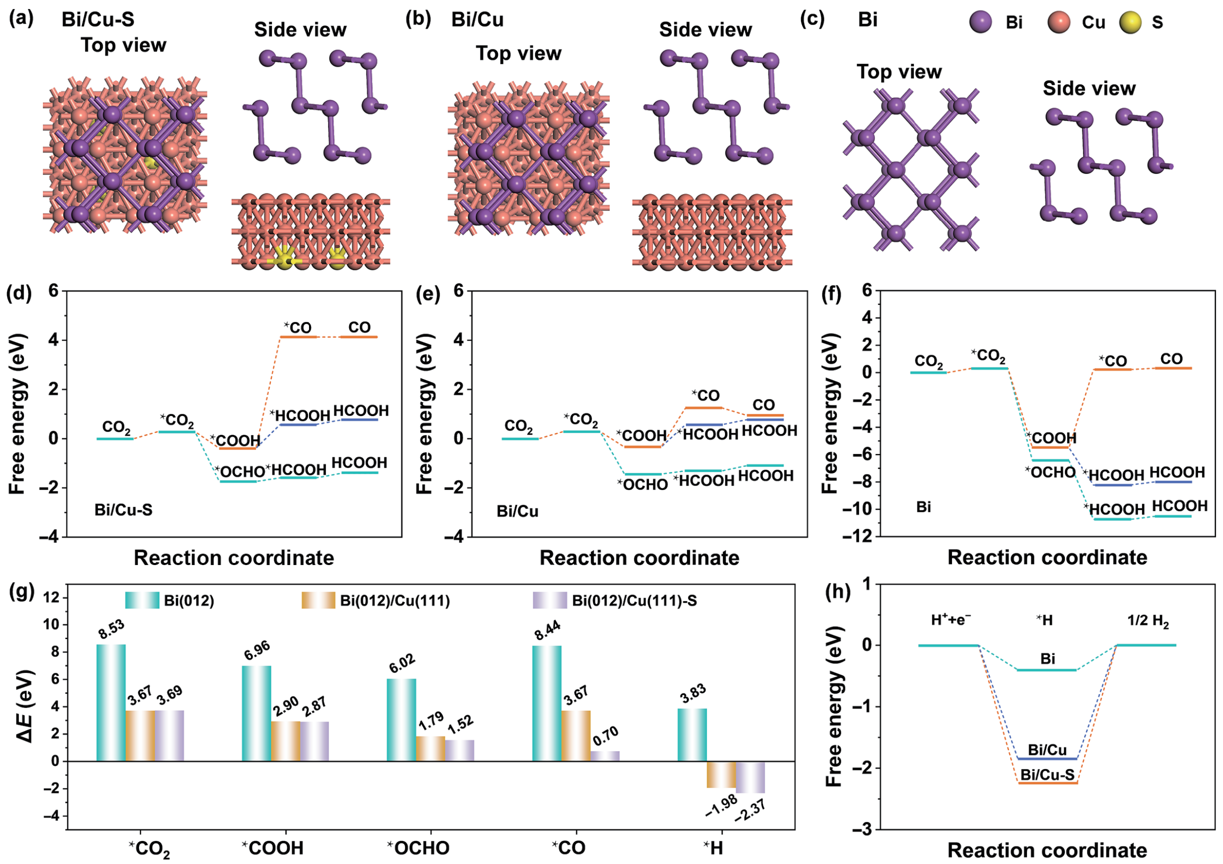

Figure 6 Top and side views of atomic models for (a) Bi(012)/Cu(111)-S, (b) Bi(012)/Cu(111), and (c) Bi(012). Reaction Gibbs free energy diagrams of (d) Bi (012)/Cu(111)-S, (e) Bi(012)/Cu(111), and (f) Bi(012) toward HCOOH and CO. (g) Adsorption energies of CO_2, *COOH, *OCHO, *CO, and *H over Bi(012)/Cu(111)-S, Bi (012)/Cu(111), and Bi(012). (h) Reaction Gibbs free energy diagram toward H_2.

4.0% (Table S5 and Fig. S8 in the ESM), which is slightly reduced compared with the S content of 4.3% before the reaction. The results indicate that Bi/Cu-S/BM is stable.

4 Conclusions

In this work, Bi is electrodeposited on the surface of Cu-S/BM nanowires obtained from CuS/BM by electroreduction to form Bi/Cu-S/BM electrode materials for ECO_2RR. At −0.9 V, the FE of $HCOO^-$ reached the highest of 94.3% with the partial current density of −50.7 $mA{\cdot}cm^{-2}$ and the yield of 30.7 $mmol{\cdot}h^{-1}{\cdot}cm^{-2}$. Bi/Cu-S/BM also demonstrates excellent stability, with the FE of $HCOO^-$ remaining stable above 93% at −0.9 V following a reaction of 10 h and the structure also remaining stable. Theoretical calculation results show that Bi/Cu-S, Bi/Cu, and Bi structures inhibit the formation of CO, while the Bi/Cu-S structure promotes the adsorption of CO_2 and greatly enhances the adsorption of *H, which effectively inhibits HER and thus promotes the selective conversion of CO_2 to formate. The work provides a new approach for the enhanced performance of bimetallic Bi-Cu and S-modified Cu-based electrocatalysts for selective formate generation in ECO_2RR, deepening the understanding of the mechanism.

Acknowledgements

This work was supported by the National Natural Science Foundation of China (Nos. 22278020 and 2177060378), the Program for Changjiang Scholars, Innovative Research Teams in Universities (No. IRT1205), and the Fundamental Research Funds for the Central Universities (Nos. 12060093063 and XK1803-05).

Electronic Supplementary Material: Supplementary material (computational details, EDS results, SEM images and elemental mapping, Cu LMM Auger electron spectroscopy, comparison of performance, CV curves, Nyquist plots, and XRD spectra) is available in the online version of this article at https://doi.org/10.1007/s12274-023-6247-0.

References

[1] Shi, C. F.; Zhi, J. Q.; Yao, X.; Zhang, H.; Yu, Y.; Zeng, Q. S.; Li, L. J.; Zhang, Y. X. How can China achieve the 2030 carbon peak goal—A crossover analysis based on low-carbon economics and deep learning. *Energy* **2023**, *269*, 126776.

[2] Samset, B. H.; Fuglestvedt, J. S.; Lund, M. T. Delayed emergence of a global temperature response after emission mitigation. *Nat. Commun.* **2020**, *11*, 3261.

[3] Zhang, T. T.; Shang, H. S.; Zhang, B.; Yan, D. P.; Xiang, X. Ag/ultrathin-layered double hydroxide nanosheets induced by a self-redox strategy for highly selective CO_2 reduction. *ACS Appl. Mater. Interfaces* **2021**, *13*, 16536–16544.

[4] Zhang, J. Z.; Shi, J. J.; Tao, S.; Wu, L.; Lu, J. Cu_2O/Ti_3C_2MXene heterojunction photocatalysts for improved CO_2 photocatalytic reduction performance. *Appl. Surf. Sci.* **2021**, *542*, 148685.

[5] Francke, R.; Schille, B.; Roemelt, M. Homogeneously catalyzed electroreduction of carbon dioxide-methods, mechanisms, and catalysts. *Chem. Rev.* **2018**, *118*, 4631–4701.

[6] Zhang, J. F.; Li, Z. Y.; Cai, R.; Zhang, T. Y.; Yang, S. Z.; Ma, L.; Wang, Y.; Wu, Y. C.; Wu, J. J. Switching CO_2 electroreduction selectivity between C_1 and C_2 hydrocarbons on Cu gas-diffusion electrodes. *Energy Environ. Mater.* **2023**, *6*, e12307.

[7] Gao, D.; Yang, J. X.; Qi, Y. W.; Guo, C.; Zhang, H. Review and perspectives on CO_2 bubble dynamic characteristics in different liquids during carbon capture, utilization, and storage process. *Energy Fuels* **2023**, *37*, 58–73.

[8] Dou, T.; He, J. Q.; Diao, S. T.; Wang, Y. P.; Zhao, X. H.; Zhang, F. Z.; Lei, X. D. Dynamic reconstructuring of CuS/SnO_2-S for

promoting CO_2 electroreduction to formate. *J. Energy Chem.* **2023**, *82*, 497–506.

[9] Alli, Y. A.; Oladoye, P. O.; Ejeromedoghene, O.; Bankole, O. M.; Alimi, O. A.; Omotola, E. O.; Olanrewaju, C. A.; Philippot, K.; Adeleye, A. S.; Ogunlaja, A. S. Nanomaterials as catalysts for CO_2 transformation into value-added products: A review. *Sci. Total Environ.* **2023**, *868*, 161547.

[10] Gao, T. F.; Kumar, A.; Shang, Z. C.; Duan, X. X.; Wang, H. C.; Wang, S. Y.; Ji, S. F.; Yan, D. P.; Luo, L.; Liu, W. et al. Promoting electrochemical conversion of CO_2 to formate with rich oxygen vacancies in nanoporous tin oxides. *Chin. Chem. Lett.* **2019**, *30*, 2274–2278.

[11] Saeidi, S.; Amin, N. A. S.; Rahimpour, M. R. Hydrogenation of CO_2 to value-added products—A review and potential future developments. *J. CO_2 Util.* **2014**, *5*, 66–81.

[12] Du, J.; Chen, A. B. Ni nanoparticles confined by yolk–shell structure of CNT-mesoporous carbon for electrocatalytic conversion of CO_2: Switching CO to formate. *J. Energy Chem.* **2022**, *70*, 224–229.

[13] Liu, X.; Fang, Z. Y.; Teng, X.; Niu, Y. L.; Gong, S. Q.; Chen, W.; Meyer, T. J.; Chen, Z. F. Paired formate and H_2 productions via efficient bifunctional Ni-Mo nitride nanowire electrocatalysts. *J. Energy Chem.* **2022**, *72*, 432–441.

[14] Yan, W. R.; Zhang, J.; Lu, S. F.; Jiang, S. P.; Xiang, Y. Tuning dehydrogenation behavior of formic acid on boosting cell performance of formic acid fuel cell at elevated temperatures. *J. Power Sources* **2022**, *544*, 231877.

[15] Lee, C. H.; Kanan, M. W. Controlling H^+ vs. CO_2 reduction selectivity on Pb electrodes. *ACS Catal.* **2015**, *5*, 465–469.

[16] Ji Jang, H.; Hyun Yang, J.; Young Maeng, J.; Jun Kim, Y.; Kyun Rhee, C.; Sohn, Y. Electrochemical CO_2 reduction over Pb electrodes modified with group 10, 11, and 14 elements. *Appl. Surf. Sci.* **2022**, *604*, 154438.

[17] Tsujiguchi, T.; Kawabe, Y.; Jeong, S.; Ohto, T.; Kukunuri, S.; Kuramochi, H.; Takahashi, Y.; Nishiuchi, T.; Masuda, H.; Wakisaka, M. et al. Acceleration of electrochemical CO_2 reduction to formate at the Sn/reduced graphene oxide interface. *ACS Catal.* **2021**, *11*, 3310–3318.

[18] Wu, Y. Z.; Zhai, P. L.; Cao, S. Y.; Li, Z. W.; Zhang, B.; Zhang, Y. T.; Nie, X. W.; Sun, L. C.; Hou, J. G. Beyond d orbits: Steering the selectivity of electrochemical CO_2 reduction via hybridized sp band of sulfur-incorporated porous Cd architectures with dual collaborative sites. *Adv. Energy Mater.* **2020**, *10*, 2002499.

[19] Li, Z. Q.; Sun, B.; Xiao, D. F.; Wang, Z. Y.; Liu, Y. Y.; Zheng, Z. K.; Wang, P.; Dai, Y.; Cheng, H. F.; Huang, B. B. Electron-rich Bi nanosheets promote $CO_2^{\cdot-}$ formation for high-performance and pH-universal electrocatalytic CO_2 reduction. *Angew. Chem., Int. Ed.* **2023**, *62*, e202217569.

[20] Wu, M. G.; Xu, B. L.; Zhang, Y. F.; Qi, S. H.; Ni, W.; Hu, J.; Ma, J. M. Perspectives in emerging bismuth electrochemistry. *Chem. Eng. J.* **2020**, *381*, 122558.

[21] Peng, L. W.; Wang, Y. F.; Wang, Y. X.; Xu, N. N.; Lou, W. S.; Liu, P. X.; Cai, D. Q.; Huang, H. T.; Qiao, J. L. Separated growth of Bi-Cu bimetallic electrocatalysts on defective copper foam for highly converting CO_2 to formate with alkaline anion-exchange membrane beyond $KHCO_3$ electrolyte. *Appl. Catal. B: Environ.* **2021**, *288*, 120003.

[22] Zu, M. Y.; Zhang, L.; Wang, C. W.; Zheng, L. R.; Yang, H. G. Copper-modulated bismuth nanocrystals alter the formate formation pathway to achieve highly selective CO_2 electroreduction. *J. Mater. Chem. A* **2018**, *6*, 16804–16809.

[23] Deng, Y. L.; Huang, Y.; Ren, D.; Handoko, A. D.; Seh, Z. W.; Hirunsit, P.; Yeo, B. S. On the role of sulfur for the selective electrochemical reduction of CO_2 to formate on CuS_x catalysts. *ACS Appl. Mater. Interfaces* **2018**, *10*, 28572–28581.

[24] Dou, T.; Qin, Y.; Zhang, F. Z.; Lei, X. D. CuS nanosheet arrays for electrochemical CO_2 reduction with surface reconstruction and the effect on selective formation of formate. *ACS Appl. Energy Mater.* **2021**, *4*, 4376–4384.

[25] Qin, Y.; Kong, X. G.; Lei, D. Q.; Lei, X. D. Facial grinding method for synthesis of high-purity CuS nanosheets. *Ind. Eng. Chem. Res.* **2018**, *57*, 2759–2764.

[26] Morales-García, A.; Soares, A. L. Jr; Dos Santos, E. C.; de Abreu, H. A.; Duarte, H. A. First-principles calculations and electron density topological analysis of covellite (CuS). *J. Phys. Chem. A* **2014**, *118*, 5823–5831.

[27] Conejeros, S.; Moreira, I. D. P. R.; Alemany, P.; Canadell, E. Nature of holes, oxidation states, and hypervalency in covellite (CuS). *Inorg. Chem.* **2014**, *53*, 12402–12406.

[28] Singh, H.; Kumar, S.; Sharma, P. K. Tunable exciton–plasmon coupled resonances with Cu^{2+}/Cu^{+} substitution in self-assembled CuS nanostructured films. *Appl. Surf. Sci.* **2023**, *612*, 155831.

[29] Guo, P. P.; He, Z. H.; Yang, S. Y.; Wang, W. T.; Wang, K.; Li, C. C.; Wei, Y. Y.; Liu, Z. T.; Han, B. X. Electrocatalytic CO_2 reduction to ethylene over ZrO_2/Cu-Cu_2O catalysts in aqueous electrolytes. *Green Chem.* **2022**, *24*, 1527–1533.

[30] DeSario, P. A.; Pietron, J. J.; Brintlinger, T. H.; McEntee, M.; Parker, J. F.; Baturina, O.; Stroud, R. M.; Rolison, D. R. Oxidation-stable plasmonic copper nanoparticles in photocatalytic TiO_2 nanoarchitectures. *Nanoscale* **2017**, *9*, 11720–11729.

[31] Ding, S. Q.; Liu, S.; Li, J. J.; Wu, L.; Ma, Z. F.; Yuan, X. X. Multifunctional catalyst CuS for nonaqueous rechargeable lithium-oxygen batteries. *ACS Appl. Mater. Interfaces* **2021**, *13*, 50065–50075.

[32] Yang, C.; Hu, Y. R.; Li, S. X.; Huang, Q.; Peng, J. Self-supporting Bi-Sb bimetallic nanoleaf for electrochemical synthesis of formate by highly selective CO_2 reduction. *ACS Appl. Mater. Interfaces* **2023**, *15*, 6942–6950.

[33] Dou, T.; Du, J. W.; He, J. Q.; Wang, Y. P.; Zhao, X. H.; Zhang, F. Z.; Lei, X. D. Sulfurization-derived Cu^0-Cu^+ sites for electrochemical CO_2 reduction to ethanol. *J. Power Sources* **2022**, *533*, 231393.

[34] Hu, Q. F.; Liu, Y.; Zheng, X. R.; Zhang, J. F.; Wang, J. J.; Han, X. P.; Deng, Y. D.; Hu, W. B. How the surface Cu layer affected the activity of Ni foil for alkaline hydrogen evolution. *J. Mater. Sci. Technol.* **2024**, *169*, 11–18.

[35] Fan, B.; Zhou, B. N.; Chen, S.; Zhu, F. X.; Chen, B.; Gong, Z. M.; Wang, X. L.; Zhu, C. Y.; Zhou, D. M.; He, F. et al. Preparation of Fe/Cu bimetals by ball milling iron powder and copper sulfate for trichloroethylene degradation: Combined effect of FeS_x and Fe/Cu alloy. *J. Hazard. Mater.* **2023**, *460*, 132402.

[36] Azenha, C.; Mateos-Pedrero, C.; Alvarez-Guerra, M.; Irabien, A.; Mendes, A. Binary copper-bismuth catalysts for the electrochemical reduction of CO_2: Study on surface properties and catalytic activity. *Chem. Eng. J.* **2022**, *445*, 136575.

[37] Chang, S.; Xuan, Y. M.; Duan, J. J.; Zhang, K. High-performance electroreduction CO_2 to formate at Bi/nafion interface. *Appl. Catal. B: Environ.* **2022**, *306*, 121135.

[38] Koh, J. H.; Won, D. H.; Eom, T.; Kim, N. K.; Jung, K. D.; Kim, H.; Hwang, Y. J.; Min, B. K. Facile CO_2 electro-reduction to formate via oxygen bidentate intermediate stabilized by high-index planes of Bi dendrite catalyst. *ACS Catal.* **2017**, *7*, 5071–5077.

[39] Xing, Y. L.; Kong, X. D.; Guo, X.; Liu, Y.; Li, Q. Y.; Zhang, Y. Z.; Sheng, Y. L.; Yang, X. P.; Geng, Z. G.; Zeng, J. Bi@Sn core–shell structure with compressive strain boosts the electroreduction of CO_2 into formic acid. *Adv. Sci.* **2020**, *7*, 1902989.

[40] Zhao, M. M.; Gu, Y. L.; Gao, W. C.; Cui, P. X.; Tang, H.; Wei, X. Y.; Zhu, H.; Li, G. Q.; Yan, S. C.; Zhang, X. Y. et al. Atom vacancies induced electron-rich surface of ultrathin Bi nanosheet for efficient electrochemical CO_2 reduction. *Appl. Catal. B: Environ.* **2020**, *266*, 118625.

[41] Sui, P. F.; Xu, C. Y.; Zhu, M. N.; Liu, S. B.; Liu, Q. X.; Luo, J. L. Interface-induced electrocatalytic enhancement of CO_2-to-formate conversion on heterostructured bismuth-based catalysts. *Small* **2022**, *18*, 2105682.

[42] Liu, S. B.; Lu, X. F.; Xiao, J.; Wang, X.; Lou, X. W. Bi_2O_3 nanosheets grown on multi-channel carbon matrix to catalyze efficient CO_2 electroreduction to HCOOH. *Angew. Chem., Int. Ed.* **2019**, *58*, 13828–13833.

[43] Allioux, F. M.; Merhebi, S.; Ghasemian, M. B.; Tang, J. B.; Merenda, A.; Abbasi, R.; Mayyas, M.; Daeneke, T.; O'Mullane, A. P.; Daiyan, R. et al. Bi-Sn catalytic foam governed by nanometallurgy of liquid metals. *Nano Lett.* **2020**, *20*, 4403–4409.

[44] Liu, B. W.; Xie, Y.; Wang, X. L.; Gao, C.; Chen, Z. M.; Wu, J.;

Meng, H. Y.; Song, Z. C.; Du, S. C.; Ren, Z. Y. Copper-triggered delocalization of bismuth p-orbital favours high-throughput CO_2 electroreduction. *Appl. Catal. B: Environ.* **2022**, *301*, 120781.

[45] Zhang, X. L.; Sun, X. H.; Guo, S. X.; Bond, A. M.; Zhang, J. Formation of lattice-dislocated bismuth nanowires on copper foam for enhanced electrocatalytic CO_2 reduction at low overpotential. *Energy Environ. Sci.* **2019**, *12*, 1334–1340.

[46] Hu, Y. J.; Lu, D. Z.; Zhou, W. L.; Wang, X. Y.; Li, Y. Y. *In situ* construction of 3D low-coordinated bismuth nanosheets@Cu nanowire core–shell nanoarchitectures for superior CO_2 electroreduction activity. *J. Mater. Chem. A* **2023**, *11*, 1937–1943.

[47] Zhang, F. H.; Chen, C. Z.; Yan, S. L.; Zhong, J. H.; Zhang, B.; Cheng, Z. M. Cu@Bi nanocone induced efficient reduction of CO_2 to formate with high current density. *Appl. Catal. A: Gen.* **2020**, *598*, 117545.

[48] Wu, Z. D.; Yu, J.; Wu, K.; Song, J. J.; Gao, H. W.; Shen, H. L.; Xia, X. F.; Lei, W.; Hao, Q. L. Ultrafine CuS anchored on nitrogen and sulfur Co-doped graphene for selective CO_2 electroreduction to formate. *Appl. Surf. Sci.* **2022**, *575*, 151796.

[49] Kahsay, A. W.; Ibrahim, K. B.; Tsai, M. C.; Birhanu, M. K.; Chala, S. A.; Su, W. N.; Hwang, B. J. Selective and low overpotential electrochemical CO_2 reduction to formate on CuS decorated CuO heterostructure. *Catal. Lett.* **2019**, *149*, 860–869.

[50] Zhuang, T. T.; Liang, Z. Q.; Seifitokaldani, A.; Li, Y.; De Luna, P.; Burdyny, T.; Che, F. L.; Meng, F.; Min, Y. M.; Quintero-Bermudez, R. et al. Steering post-C–C coupling selectivity enables high efficiency electroreduction of carbon dioxide to multi-carbon alcohols. *Nat. Catal.* **2018**, *1*, 421–428.